International Communications in Heat and Mass Transfer 149 (2023) 107155

Contents lists available at ScienceDirect

International Communications in Heat and Mass Transfer

journal homepage: www.elsevier.com/locate/ichmt

Irreversibilities and heat transfer in magnetohydrodynamic microchannel flow under differential heating

Haroun Ragueb [a,*], Antar Tahiri [b], Dounya Behnous [c], Belkacem Manser [a], Kamel Rachedi [d], Kacem Mansouri [a]

[a] Laboratory of Energy and Mechanical Engineering (LEMI), Faculty of Technology, University M'Hamed Bougara of Boumerdes (UMBB), 35000 Boumerdes, Algeria
[b] Laboratory of Mechanical and Materials Development, LDMM, University of Djelfa, Djelfa 17000, Algeria
[c] Laboratory of Physical Engineering of Hydrocarbons, Faculty of Hydrocarbons and Chemistry, University M'Hamed Bougara of Boumerdes (UMBB), 35000 Boumerdes, Algeria
[d] Motor Dynamics and Vibroacoustics Laboratory, Faculty of Technology, University M'Hamed Bougara of Boumerdes (UMBB), 35000 Boumerdes, Algeria

ARTICLE INFO

Keywords:
Magnetohydrodynamic (MHD)
Microchannel
Entropy generation
Viscous dissipation
Joule heating
Energy efficiency

ABSTRACT

This study investigates heat transfer and entropy generation in a microchannel subjected to differential heating, viscous dissipation, and Joule heating within a magnetohydrodynamic (MHD) fluid flow. A finite difference method with a fully implicit scheme is employed to accurately model temperature distribution and entropy generation. A comparison between the average Nusselt numbers (*Nu*) calculated using the classical method and the Bennett Formula reveals a notable discrepancy, particularly at the entry length (up to 14%). It has been found that when one plate is heated while the other is cooled and the Hartmann number (*Ha*) is low, the average *Nu* for both plates converges to 2. However, at high *Ha* values considering viscous dissipation and Joule heating, there is an 8% deviation between the *Nu* values of the two plates, with the higher *Nu* found on the cooling plate. Sensitivity analyses explore the impact of control parameters on entropy generation, emphasizing the significance of η as a key parameter that reflects the system's resistance to entropy generation. Increasing η from 0.1 to 0.5 results in a 32% reduction in entropy generation. In particular, for microchannels, substantial η high values imply reduced entropy generation, highlighting their efficiency in heat transfer.

1. Introduction

The outstanding ability of microchannels to significantly improve heat transfer efficiency, despite their small and compact dimensions, has recently attracted a lot of interest [1]. A considerable amount of research has been devoted to examining the heat transfer properties of micro-sized devices, such as microsensors [2] and micropumps [3], which find crucial applications in improving device efficiency and cooling [4]. The main distinguishing property of microchannels is their characteristic length, also known as the hydraulic diameter, which ranges from a few micrometers to many hundreds of micrometers, often lying below the 1-mm threshold. This diminutive characteristic length yields intriguing heat and transport phenomena. The first of them is dependent on the Knudsen number (*Kn*), a dimensionless parameter reflecting the ratio of the molecular mean free path to the characteristic length. When the Knudsen number is <0.01, it signifies a continuum flow regime, while a Knudsen number exceeding 10 corresponds to the regime of free-molecular flow. When the Knudsen number falls within this range, from 0.01 to 10, it results in slip flow [5,6] for *Kn* values are <0.1 and transitions to the transitional flow regime when *Kn* surpasses 0.1 [7]. Liquid flow within microchannels typically conforms to the continuum flow regime due to the exceedingly small mean free path of liquid molecules, often on the order of angstroms, which leads to the emergence of remarkably low Knudsen numbers (*Kn* < <0.01) [8]. Another significant phenomenon that takes place within microchannels, closely tied to their characteristic length also, is viscous dissipation. This phenomenon depends on the Brinkman number (*Br*), and it becomes more pronounced as *Br* increases. It is worth highlighting that the Brinkman number is inversely proportional to the characteristic length, hence its importance in microchannel applications. The presence of viscous heating as an additional heat source introduces a noteworthy alteration to the heat transfer process [9].

Due to its simplicity and lack of moving components, magnetohydrodynamic (MHD) flow in microchannels presents an appealing option

* Corresponding author.
E-mail address: h.ragueb@univ-boumerdes.dz (H. Ragueb).

https://doi.org/10.1016/j.icheatmasstransfer.2023.107155

Available online 18 November 2023

for miniaturization. MHD is perfect for a variety of applications because it allows precise control of fluid flow in microscale systems by utilizing electromagnetic forces [10]. Hence, it has captured the interest of numerous scholars and opened pathways to various practical applications [11–14]. This technique has the potential to simplify the design and operation of microchannel-based devices as it has the potential to create pressure driven flow [15], and control the fluid movement without mechanical valves [16,17]. The utilization of MHD techniques introduces an auxiliary heat source, generally known as Joule heating. This phenomenon can substantially modify the temperature distribution within the fluid and influence the heat transfer processes. Consequently, several scholars has exhibited keen interest of MHD flow due to its potential to introduce transformative effects on fluid temperature distribution and heat transfer dynamics. Mousavi et al. [18] investigated the impact of viscous heating and Joule heating on the heat transfer characteristics of Al_2O_3-water nanofluid laminar flow within microchannels in the presence of a magnetic field. They employed numerical modeling techniques and found that while the effects of temperature-induced viscosity changes were negligible without a magnetic field, they became significant when a magnetic field was applied. Li et al. [19] analyzed the flow field and heat transfer in a microchannel with surface hydrophobicity and varying thickness, while subjecting it to a partial magnetic field with Hartmann numbers ranging from 0 to 30. They found that at *Ha* is set equal to 0, both viscous dissipation and heat transfer decreased as the slip coefficient increased, and increasing *Ha* resulted in an increase in the friction coefficient. In addition, the Nusselt number reached its maximum value at $Ha = 20$ for all cases, but beyond that point, increasing *Ha* led to a reduction in average *Nu*. Akinshilo [20] investigated mixed convective magnetohydrodynamic fluid flow through a vertical porous channel with radiation effects. The author examined the impact of rheological parameters, pressure gradient, Reynolds number, and radiation parameter, on heat and mass transfer. The results revealed that an increase in pressure led to higher velocity distribution, particularly towards the center of the flow channel, while an increase in the radiation parameter resulted in decreased temperature distribution, with a more significant effect near the electrically conducting wall. Pordanjani et al. [21] examined heat transfer and fluid flow in a MHD nanofluid flow within a two-parallel-plate microchannel containing three isothermal heat sources. Their findings revealed that increasing the Reynolds number (*Re*) boosted heat transfer under both slip and non-slip conditions, while viscous dissipation reduced heat transfer. Additionally, a higher slip coefficient increased the Nusselt number, especially at higher *Ha*, with a 52% increase observed.

Kalteh and Abedinzadeh [22] analyzed the flow and heat transfer of a water-Al_2O_3 nanofluid in a two-dimensional microchannel influenced by a uniform magnetic field. Using the Lattice Boltzmann method, they studied the impact of parameters such as Reynolds number, nanoparticle volume fraction, and Hartmann number on heat transfer coefficient and friction factor. They found that increasing the Reynolds number from 5 to 25 improved microchannel heat transfer performance by 19%, while the magnetic field had a limited effect on heat transfer but increased the friction factor by up to 86%. Qomi et al. [23] conducted a numerical study on a micochannel with two heat sources and a hybrid nanofluid flow, aiming to improve micro cooling efficiency. They found that increasing the strength of the magnetic field or the Reynolds number enhanced heat transfer by factors of 3.5 and 1.2, respectively. Sayed et al. [24] investigated the impact of electromagnetic hydrodynamic (EMHD) flow of single-walled carbon nanotubes (SWCNTs)-nanofluid in a microchannel with corrugated walls. Their findings indicated that the presence of SWCNTs reduced fluid velocity at the channel center, providing resistance to fluid motion, while the concentration of SWCNTs enhanced heat transfer rates. Gireesha et al. [25] considered the flow of a Williamson fluid in a microchannel, taking into account factors such as thermal radiation, heat source, slip regime, and convective boundary. The results showed that increasing the Weissenberg number and Reynolds number led to an increase in the Nusselt number, indicating enhanced heat transfer. Yang et al. [26] studied the heat transfer characteristics of magnetohydrodynamic electroosmotic flow in a two-dimensional rectangular microchannel. It has been found that when a lateral electric field is applied, an increase in the Hartmann number leads to a changing pattern in both the velocity and temperature profiles, characterized by initial increases followed by decreases. This transition point is defined as the critical Hartmann number. In contrast, the Nusselt number profile exhibits an opposing trend under these conditions.

The phenomenon of entropy generation, a fundamental concept in thermodynamics, underscores the irreversibility and inefficiency of real-world processes [27]. Its impact is far-reaching, affecting the performance and efficiency of various systems, from heat engines [28,29] to chemical reactions [30,31]. Fluid dynamics involves fundamental irreversible processes, such as liquid viscosity, system interactions, Joule heating, etc. [32–35]. Recognizing the importance of entropy optimization, numerous scholars have devoted their efforts to minimizing entropy generation, aiming to enhance the efficiency and sustainability of diverse technological and industrial applications of microchannels. Puttaswmay and Jayanna [36] investigated the entropy generation and heat transfer of the magnetohydrodynamic flow of a water-based Al_2O_3-CuO_3 hybrid nanoliquid through a vertical microchannel with consideration of thermal radiation. They found that the radiation parameter and nanoparticle volume fraction reduced the thermal energy of the hybrid nanofluid, and entropy generation decreased with the Hartmann number but increased with the Grashof number and Biot number. Gireesha et al. [37] investigated the impact of magnetic fields, suction/injection, and convective boundary conditions on heat transfer and entropy generation in a conducting Casson fluid flowing through an inclined porous microchannel, considering temperature-dependent heat sources. Results showed that the entropy generation rate decreases near the channel walls with an increase in the Hartmann number but increases in the central region of the microchannel. Hosseini et al. [38] analyzed the entropy generation in a horizontal porous microchannel heated symmetrically with water and Al_2O_3 nanoparticles. They analyzed the influence of the magnetohydrodynamic field, solid heat generation, and symmetric thermal conditions. The findings showed that the MHD field significantly affected temperature and velocity distributions and, consequently, reduced heat transfer irreversibilities. The study also identified an optimum Reynolds number of 6.5 for minimizing total entropy generation when other parameters were held constant. Khan et al. [39] focused on entropy optimization in the context 2D flow of non-Newtonian liquid over a stretched surface with convective boundary conditions and consideration for viscous dissipation. They observed that entropy generation was higher for higher values of *Ec* and *Ha*, while it had the opposite effect with certain material parameter called *M* [39].

Madhu et al. [40] investigated entropy production in the fully-developed heat transport of non-Newtonian Carreau fluid in an inclined microchannel, considering Roseland thermal radiation and viscous heating. They used mathematical modeling with the Finite Element Method and found that entropy generation decreased at the left and right phases of the channel, while the Bejan number increased at both phases and reached its maximum at the center of the channel with increasing Weissenberg number. In a second paper [41], the authors conducted an analysis of entropy generation and heat transfer of MHD third-grade fluid flow through a vertical porous microchannel with convective boundary conditions. The study found that entropy production could be enhanced through convective heating and viscous dissipation. Noreen et al. [42] conducted entropy production analysis for the electroosmotically assisted peristaltic flow of EMHD water-based nanofluids through a porous asymmetric microchannel. The results showed that entropy generation was influenced by various parameters such as the Hartmann number, Eckert number an others, while it decreased with permeability of the porous medium. Rao et al. [43] conducted an analysis of entropy production in the context of hybrid

nanofluid flow through a vertical microchannel. They observed that as the Brinkman and Dufour numbers increased, there were significant changes in the entropy production rate. This suggests that these parameters have a notable impact on the thermodynamic irreversibilities associated with the flow.

In this study, the novelty lies in the comprehensive exploration of entropy generation and heat transfer dynamics within a magnetohydrodynamic (MHD) flow system in the context of a parallel plate microchannel subjected to differential heating. The applied heat flux distributions have a notable impact the thermal response [44]. What sets this research apart is its practical significance, as it mirrors real-world scenarios, for instance, where one wall is actively heating while the other wall is poorly insulated (heat leaking), or instances of dual-wall heating with varying heat fluxes due to inadequate control mechanisms. This investigation is crucial for the design of energy-efficient equipment and predicting the performance of aging or suboptimal systems, highlighting its unique contribution to the field of heat transfer and entropy generation. The subsequent section presents the problem statement and mathematical formulations, whereas section 3 delves into the modeling of entropy generation. Section 5 provides insights into the numerical methodology employed, along with a sensitivity analysis of the developed computational code. Section 6 presents our key findings, followed by a comprehensive conclusion.

2. Problem statement

Consider a rectangular microchannel that satisfies the condition of having a width considerably greater than its height, which allows us to model the flow occurring within using the parallel plates approach [45]. These plates are parallel to the *xz*-plane, separated by a distance denoted *l*, are considered to be electrically non-conducting and thermally conducting. Within this microchannel, a fully developed laminar flow, in the *z*-axis direction, is established between the parallel plates. The Lorentz force generated due to a perpendicular magnetic field with an intensity denoted as B_0 drives this flow. The fluid possesses finite electrical conductivity and constant thermally independent physical properties. Upon entry into the channel, the fluid has a fully developed velocity profile with a uniform temperature distribution. The Fig. 1 presents schematic view of the considered problem.

In our analysis, we consider a differential heating case that means the bottom plate (referred as Plate 1) is subjected to a constant heating flux $\dot{q}_1^{''}$, whereas the top plate (referred as Plate 2) experiences a uniform heat flux $\dot{q}_2^{''}$, that could either heat or cool the fluid at a different rate compared to plate 1. The special cases of $\dot{q}_2^{''} = \dot{q}_1^{''}$ and $\dot{q}_2^{''} = 0$ are considered also. Additionally, no sleep boundary condition have been considered as well as viscose dissipation and joule heating whereas the axial conduction is neglected due to the forced convection ($Pe > 100$), hence the energy equation can be written as follow:

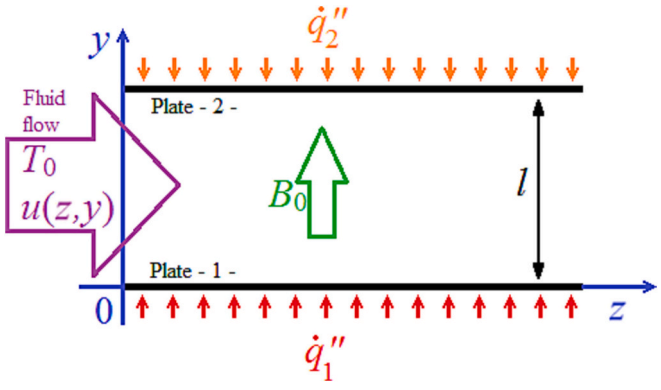

Fig. 1. Schematic representation of the microchannel and heat transfer configuration.

$$\rho c_p u\left(\frac{\partial T}{\partial z}\right) = k\left(\frac{\partial^2 T}{\partial y^2}\right) + \mu\left(\frac{\partial u}{\partial y}\right)^2 + \sigma B_0^2 u^2 \tag{1}$$

with the following boundary conditions

$$k\frac{\partial T}{\partial y}\Big|_{y=0} = \dot{q}_1^{''} = \dot{q}^{''} \tag{2}$$

$$-k\frac{\partial T}{\partial y}\Big|_{y=l} = -\dot{q}_2^{''} = -\delta\dot{q}^{''} \tag{3}$$

$$T(y, z=0) = T_0 \tag{4}$$

where $\delta = \dot{q}_2^{''}/\dot{q}_1^{''}$. When δ is set equal to 0, the upper plate operates as an adiabatic wall, If it takes on a positive value, the plate functions as a heating wall, conversely, a negative value indicates that the plate acts as a heat sink, causing the fluid to lose heat and thereby cooling it down.

To derive a comprehensive and more representative solution, the problem defined by Eqs. (1–4) is reformulated in the dimensionless form using the following dimensionless parameter:

$$Z = \frac{z}{l.Pe};\ Y = \frac{y}{l} \tag{5}$$

$$U = \frac{u}{u_{\max}};\ \theta = \frac{k(T - T_0)}{l.\dot{q}^{''}} \tag{6}$$

$$Pe = \frac{\rho c_p u_{\max} l}{k};\ Br = \frac{\mu u_{\max}^2}{l.q};\ Ha = B_0 l\sqrt{\frac{\sigma}{\mu}} \tag{7}$$

where *Pe* is the Péclet number, *Br* is the Brinkman number, and *Ha* is the Hartmann number. By substitution, the dimensionless energy equation is rewritten as follow:

$$U\left(\frac{\partial \theta}{\partial Z}\right) = \left(\frac{\partial^2 \theta}{\partial Y^2}\right) + Br\left(\frac{\partial U}{\partial Y}\right)^2 + Br.Ha^2.U^2 \tag{8}$$

with the following boundary conditions:

$$\frac{\partial \theta}{\partial Y}\Big|_{Y=0} = 1 \tag{9}$$

$$\frac{\partial \theta}{\partial Y}\Big|_{Y=1} = \delta \tag{10}$$

$$\theta(Y, Z=0) = 0 \tag{11}$$

As previously stated, given the constancy of fluid properties and the assumption of a non-slip condition at the fluid-wall interface for velocity, it is valid to employ Hartmann's velocity profile, and it is defined as follows [46,47]:

$$U(Y) = Ha\cdot\left[\frac{cosh(Ha) - cosh(Ha\cdot(2Y-1))}{Ha\cdot cosh(Ha) - sinh(Ha)}\right] \tag{12}$$

It is noteworthy to mention that when $Ha \ll 1$, the flow exhibits a parabolic profile characteristic of Poiseuille flow. In our study, we have approximated this flow by assigning a value of $Ha = 0.0001$, as going below this value can lead to a divergence due to the division by 0 in Eq. (12). This choice ensures numerical stability while preserving the accuracy of the obtained results.

Upon the completion of the resolution process, the determination of the bulk temperature is obtained using the following formula:

$$\theta_b(Z) = \frac{\int_0^1 U(Y)\cdot\theta(Y,Z)dY}{\int_0^1 U(Y)dY} \tag{13}$$

The local Nusselt number of the bottom plate (Plate 1) is given by:

$$Nu_1(Z) = \frac{1}{\theta_{w1}(Z) - \theta_b(Z)} \tag{14}$$

whereas for the top plate (Plate 2) is defined as follows:

$$Nu_2(Z) = \frac{|\delta|}{\theta_{w2}(Z) - \theta_b(Z)} \tag{15}$$

Here, $\theta_w$referrers to the temperature of corresponding wall.

For the calculation of the local Nusselt number of plate 2 (Nu_2), we have introduced the absolute value of the ratio δ. This adjustment serves the purpose of enhancing the differentiation between the heating and cooling phases. Specifically, during the cooling phase by plate 2 ($\delta < 0$, negative numerator), the wall temperature falls below the bulk temperature (negative denominator), a positive Nusselt number is yielded. Although this is correct, it fails to explicitly convey whether the fluid is undergoing heating or cooling. Consequently, by considering $|\delta|$, the Nusselt number acquires a sign: if the wall temperature is lower than the bulk temperature (indicating cooling), the Nusselt number becomes negative (the heat transfer from the fluid to the wall), effectively representing the cooling phase, and vice-versa. It is important to note that during the resolution phase, Delta can take its imposed value without the absolute sign.

Traditionally, the average Nusselt number is calculated as follow:

$$\overline{Nu}(L) = \frac{1}{L}\int_0^L Nu(Z)dZ \tag{16}$$

However, according to Bennett [48,49], there was a historical misperception in calculating the average Nusselt number in ducts subject to a constant wall heat flux. This misperception can result in an average error of 12.5% for fully developed flow. Therefore, in our study, we are following the methodology proposed by Bennett [48]. The average Nusselt number of each plate, for a given duct length L, is calculated as follows:

$$\overline{Nu_i}(L) = \frac{L}{\int_0^L \frac{dZ}{Nu_i(Z)}} \tag{17}$$

where i is the plate index ($i = 1$ or 2).

3. Evaluation of entropy generation

Once the velocity and temperature fields have been obtained, it becomes possible to assess the rate of entropy generation within the microchannel, serving as a fundamental aspect for optimization endeavors. In the context of a viscous, incompressible laminar flow, the local rate of entropy generation can be expressed as shown in Eq. (18), where three distinct sources of entropy generation are identified: the first arises from heat transfer, the second from viscous dissipation, and the third from Joule heating [27]:

$$S'''_{gen}(y,z) = \underbrace{\frac{k}{T(y,z)^2}\left[\left(\frac{\partial T(y,z)}{\partial y}\right)^2 + \left(\frac{\partial T(y,z)}{\partial z}\right)^2\right]}_{\substack{\text{Entropy generation}\\ \text{due to heat transfer}\\ \text{SHT}}} + \underbrace{\frac{\mu}{T(y,z)}\left(\frac{\partial u(y)}{\partial y}\right)^2}_{\substack{\text{Entropy generation}\\ \text{due to viscous heating}\\ \text{SVD}}} + \underbrace{\frac{\sigma B_0^2}{T(y,z)}u(y)^2}_{\substack{\text{Entropy generation}\\ \text{due to Joule heating}\\ \text{SJH}}} \tag{18}$$

By introducing dimensionless parameters defined in Eqs. (5–7), the dimensionless local entropy generation can be written as follow:

$$N_{ST}(Y,Z) = \frac{l^2}{k}S'''_{gen} = \underbrace{\frac{1}{(\theta+\eta)^2}\left[\left(\frac{\partial\theta}{\partial Y}\right)^2 + \frac{1}{Pe^2}\left(\frac{\partial\theta}{\partial Z}\right)^2\right]}_{N_{SHT}} + \underbrace{\frac{Br}{(\theta+\eta)}\left(\frac{\partial U}{\partial Y}\right)}_{N_{SVD}} + \underbrace{\frac{Br.Ha^2.U^2}{(\theta+\eta)}}_{N_{SJH}} \tag{19}$$

where

$$\eta = \frac{k\,T_0}{l\,\dot{q}''} \tag{20}$$

The dimensionless parameter given by Eq. (20), particularly denoted as η, and its physical implications, will be further elaborated upon in the subsequent discussion.

As we are considering forced convection, we make the assumption that the $Pe > 100$. This allows us to simplify Eq. (19) to the following form:

$$N_{ST}(Y,Z) = \underbrace{\frac{1}{(\theta+\eta)^2}\left(\frac{\partial\theta}{\partial Y}\right)^2}_{N_{SHT}} + \underbrace{\frac{Br}{(\theta+\eta)}\left(\frac{\partial U}{\partial Y}\right)}_{N_{SVD}} + \underbrace{\frac{Br.Ha^2.U^2}{(\theta+\eta)}}_{N_{SJH}} \tag{21}$$

Upon evaluation of the local entropy generation rate, it becomes feasible to proceed with the assessment and determination of the local Bejan number, *Be*, a fundamental parameter that serves as a crucial component in the characterization and analysis of the thermodynamic and heat transfer performance within the given system, by following the expression as outlined below [50]:

$$Be(Y,Z) = \frac{N_{SHT}}{N_{ST}} = \frac{N_{SHT}}{N_{SHT} + N_{SVD} + N_{SJH}} \tag{22}$$

Additionally, the average entropy number for each component can be calculated using the following integration formula:

$$\overline{N_{Sxx}} = \frac{1}{l\cdot L_d}\int_0^{L_d}\int_0^{l} N_{Sxx}(Y,Z)dYdZ \tag{23}$$

Consequently, the average Bejan number for the system is given by:

$$\overline{Be} = \frac{\overline{N_{SHT}}}{\overline{N_{ST}}} \tag{24}$$

4. Numerical resolution and validation

The numerical solution for the previously stated problem, as defined by Eq. (8), along with the boundary conditions presented in Eqs. (9–11), is achieved through the utilization of the finite difference method [51]. To discretize the partial differential equation, a fully implicit scheme is employed, resulting in the formulation of an algebraic system of equations with three diagonals matrices for each axial step ΔZ_i. Implicit schemes are known for their inherent stability and convergence properties, which contribute to the accuracy and reliability of the numerical

solution [52]. Eq. (8) is discretized through the implementation of three-point central differences to handle second-order derivatives, while first-order derivatives are managed using two-point forward differences. In order to have a dynamic resolution process and to accurately evaluate the heat response in the entry length of the microchannel, a variable ΔZ_i is used as follow [53]:

$$\Delta Z_{i+1} = Z_{i+1} - Z_i \tag{25}$$

where

$$Z_i = L_d \left(\frac{i}{n}\right)^r \tag{26}$$

Here, i is the discretization index along the Z-axis, n is the number of steps, r is numerical exponent and L_d represents the dimensionless length of the channel. Selecting a suitable exponent value, $r > 1$, enhances the accuracy of calculated temperature at the entrance of the duct. For this investigation, the value $r = 4$ is chosen to attain starting ΔZ_i values on the order of 10^{-10}.

The numerical resolution was obtained using an in-house code, and once the temperature field is obtained, entropy generation is calculated using second-order differences to compute the temperature derivatives. The code underwent mesh sensitivity analysis and the results were compared with literature for reliability assessment, as depicted in Fig. 2. Fig. 2a illustrates the effect of grid size on result accuracy. Three types of quadratic grids were considered: 50 × 1000, 100 × 2000, and 200 × 4000, where the first number represents discretization along the Y-axis, and the second number along the Z-axis. Additionally, a comparison is made based on the local Nusselt number using the analytical solution provided by Cotta and Özişik [54], for a Newtonian fluid, without considering viscous dissipation ($Br = 0$), along with Joule heating and Hartmann flow (Ha = 0.0001). The plates are subjected to the same heating flux ($\delta = 1$). It is evident that as the grid size increases, the deviation between our solution and Cotta and Özişik diminishes. At $Z = 10^{-6}$, the error between our solution and the analytical one is approximately 2.7%. At $Z = 10^{-5}$, this error reduces to 0.5%. Further downstream, the error continues to decrease, reaching 0.04% at $Z = 10^{-4}$ and ultimately 0.00% in the developed region where the asymptotic Nusselt number reaches 8.235. It is important to note that the Nusselt number of the system is the sum of the Nusselt numbers of each plate ($Nu = Nu_1 + Nu_2$). However, this addition is not valid when the plates have different heat fluxes. The remaining results on this paper are obtained using a grid of 200 × 4000.

In the second step, we investigate the accuracy of our code concerning Hartmann flow under a constant heat flux ($\delta = 1$), without considering viscous and Joule heating effects. The comparison is based on the asymptotic Nusselt number of the system (Nu), obtained by our code at $Z = 10$ and the analytical correlation obtained by Lahjomri et al. (refer to Eq. 49 in Ref. [55]). As observed in Fig. 2b, our results closely align with the correlation proposed by Lahjomri et al. For low values of the Hartmann number ($Ha < 40$), the error remains below 0.01%, with the maximum error reaching 0.32% at $Ha = 200$.

The Fig. 2c illustrates the asymptotic Nusselt number of both the upper and bottom plates, comparing it to the analytical correlation derived by Sheela-Francisca and Tso (refer to Eq. 21 in Ref. [56]). This comparison is made for the case of symmetric heating ($\delta = 1$), considering viscous dissipation while neglecting Joule heating ($Ha = 0.0001$).

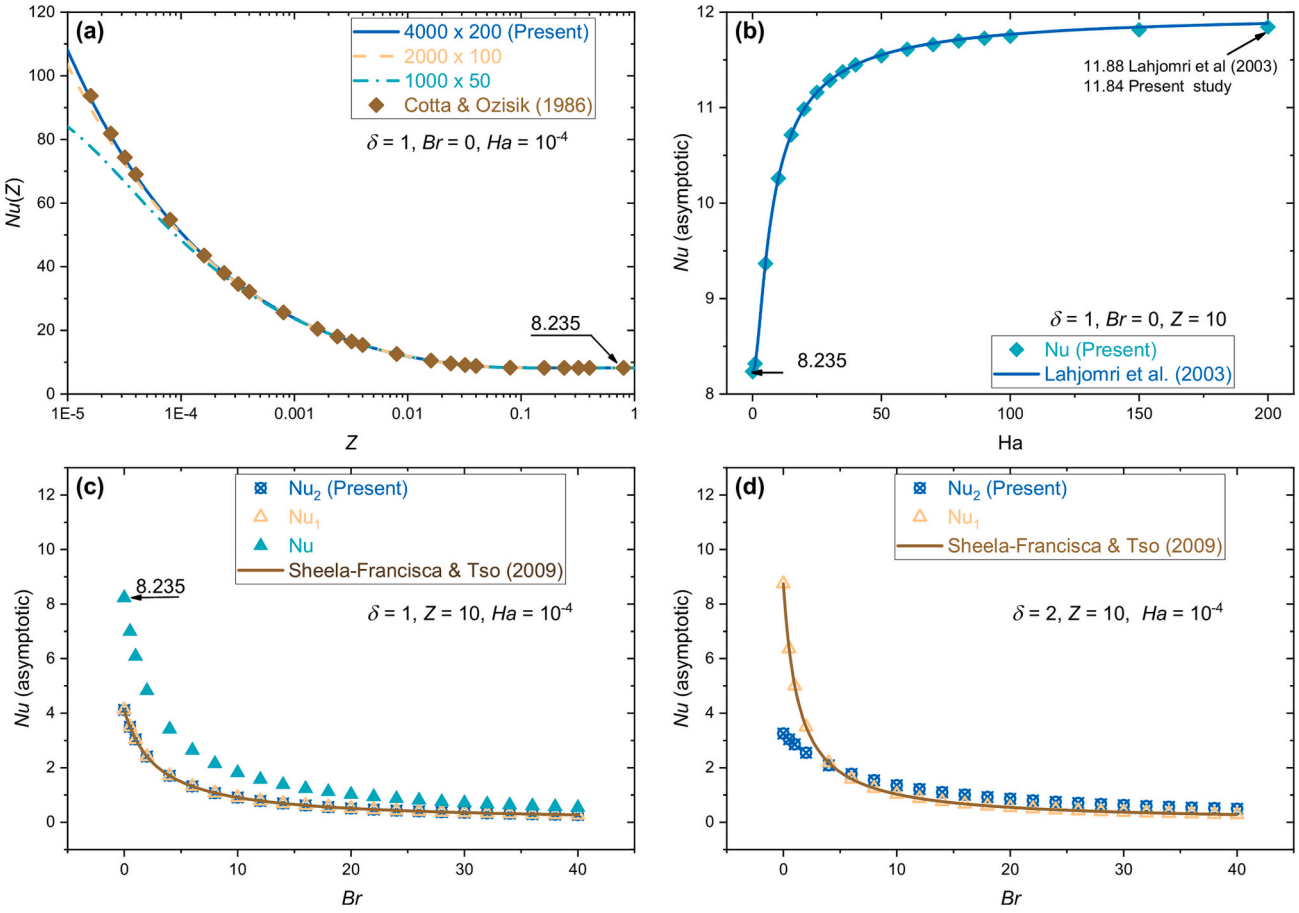

Fig. 2. Code sensitivity analysis and validation, **a)** Grid size impact on local Nusselt number deviation. **b)** Accuracy assessment of asymptotic Nusselt number for Hartmann. c) Comparison of asymptotic Nusselt numbers for symmetric heating with viscous dissipation. d) Assessment of viscous dissipation effect in case of differential heating.

As observed, our results align perfectly with the data obtained from the Sheela-Francisca and Tso correlation, with an overall error of <0.01%.

In Fig. 2d, we investigate the scenario of differential heating with viscous dissipation (Plate 2 has a higher heat flux, $\delta = 2$). Once again, our results are compared against the correlation by Sheela-Francisca and Tso [56]. As can be observed, the computed asymptotic Nusselt numbers for the bottom plate (plate 1) match those calculated using the correlation (errors <0.01%). However, the proposed correlation by Sheela-Francisca and Tso is not valid for the top plate. Plate 2 exhibits different asymptotic Nusselt numbers. For low Brinkman numbers ($Br <$ 5), its Nusselt number is lower than that of plate 1. However, for higher Brinkman numbers, it is larger than the Nusselt number of plate 1.

In summary, our developed code demonstrates remarkable accuracy in predicting local and asymptotic Nusselt numbers for various heat transfer scenarios, as highlighted in Fig. 2. The strong agreement with established correlations and literature data validates the code's reliability and accuracy.

5. Results and discussion

5.1. Heat transfer response

In the first part of this discussion, we will be interested on the effect of differential heating with consideration of viscous dissipation and Joule heating. The main purpose of this paper is to investigate the entropy generation, as the heat response for the classical symmetry heating cases has been widely discussed in literature. The only case of differential heating we know that exists in literature is the work of Sheela-Francisca and Tso [56], where the authors investigated this type of boundary condition For Graetz-Brinkman flow.

Fig. 3a illustrates the progression of the Local Nusselt number along the microchannel for three distinct Hartmann number values ($Ha =$ 0.0001, $Ha = 10$, $Ha = 40$), considering both viscosity and Joule heating under symmetric boundary conditions ($\delta = 1$). Given $\delta = 1$, the Nusselt number of the system is equal to the sum of Nu_1 and Nu_2. Notably, upon consideration of viscous and Joule heating, and for the Poiseuille flow ($Ha = 0.0001$), a slight reduction in the Nusselt number is observed in comparison to the case where $Br = 0$. This reduction is evident until it attains a value of 7.95 within the fully established region (for $Br = 0$, the asymptotic $Nu = 8.235$). With an increase in the Hartman number value, the local Nusselt number also experiences an improvement. This is due to the increase in velocity gradients near the plates, thereby enhancing heat transfer. Moreover, we have computed the average Nusselt number at a designated distance (Z) using eqs. (16) and (17), as presented in Fig. 3b. The dashed lines depict the average Nusselt number derived using the conventional approach defined by Eq. (16), while the solid lines represent the average calculated using the Bennett formula outlined in Eq. (17). Upon examining the thermally developing region, a marked distinction between the traditional average Nusselt and the Bennett average Nusselt is evident. This the error between the two equations is quantified and presented in Fig. 3c. As observable, the error between the two formulas can reach up to 14% within the developing region, marking a highly significant disparity. This divergence holds substantial implications for the design of heat-related equipment, such

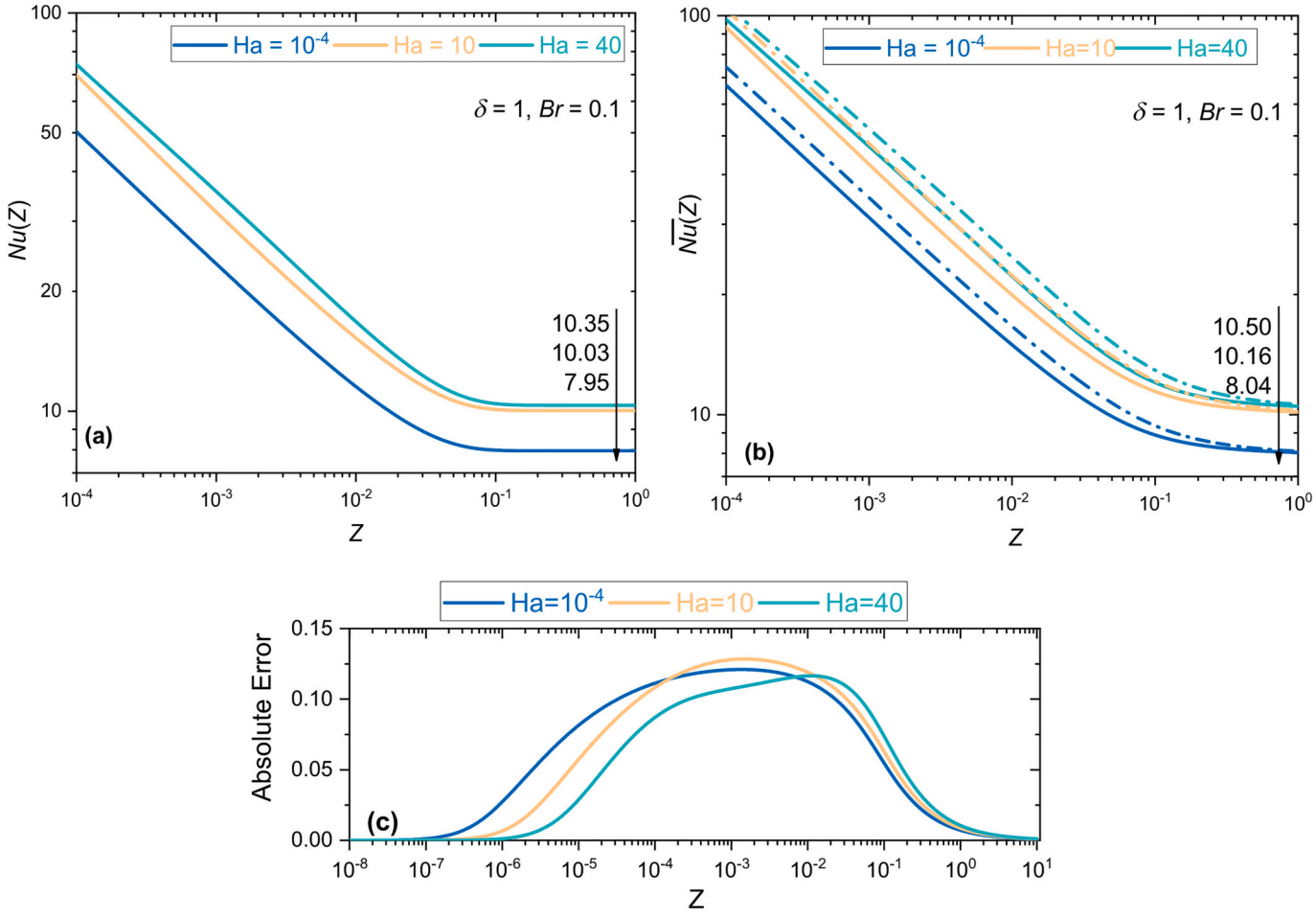

Fig. 3. a) Evolution of local Nusselt number along microchannel with viscous and joule heating. **b)** Comparison of average Nusselt numbers, classical (Eq. 16, dashed lines) vs. Bennett approach (Eq. 17, solid lines). **c)** Absolute error between classical and Bennett average Nusselt numbers. The asymptotic values in (a) and (b) are computed at $Z = 1$.

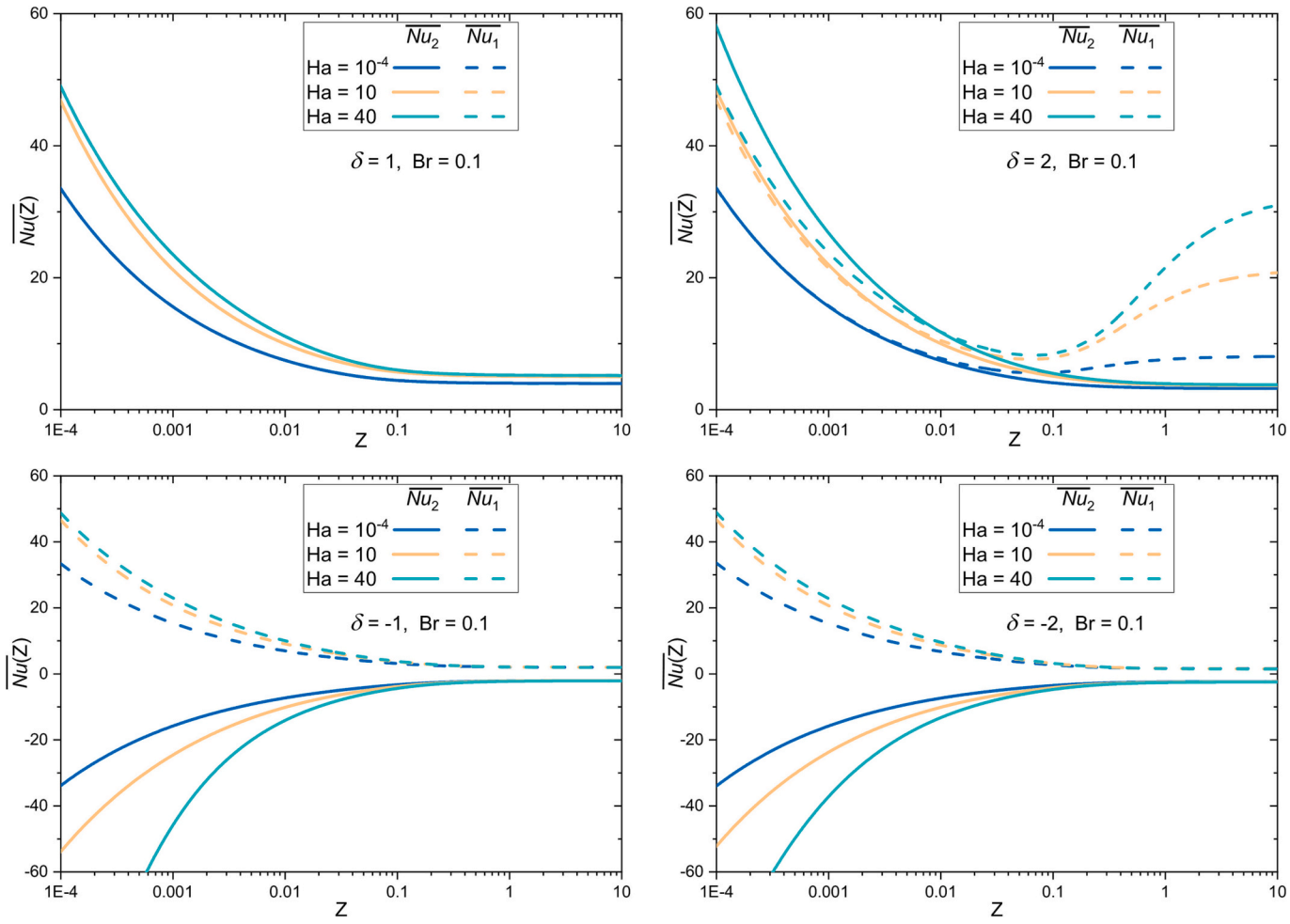

Fig. 4. Effect Heat Flux Ratio (δ) on average Nusselt numbers for upper and lower plates in with consideration of viscous and Joule heating.

as electronic coolers. The potential for inadequate performance relative to expectations could result in equipment damage over prolonged use, stemming from ineffective heat dissipation (see Eqs. 14 and 15).

Fig. 4 illustrates the impact of the heat flux ratio, δ, on the average Nusselt number of the upper and lower plates. Evidently, under symmetric heating conditions with $\delta = 1$, the average Nusselt numbers for both plates are congruent. When $\delta = 2$, i.e. the upper plate's heat flux doubles that of the lower plate, and for parabolic flow ($Ha = 0.0001$), the heat transfer in the entry region yields equal Nusselt numbers for both plates ($Z < 0.01$). However, as the Hartmann number increases, the differences in Nu between the two plates amplify, and it becomes more pronounced at $Ha = 40$. The increase in Hartmann number flattens the velocity profile at the core, augment the gradient near the walls, thus intensifying heat exchange between the plate and fluid and accentuating inter-plate deviations. In the developed region, the average Nusselt number for the upper plate converges towards an asymptotic value below that of the bottom plate. At specific axial positions, the fluid bulk temperature aligns with the bottom plate's temperature, thereby causing an increase in Nusselt number and for some cases leads to singularity point when $\theta_b \approx \theta_w$, (see Eqs. 14 and 15). Notably, the elevated Nusselt number for the bottom plate in the developed region does not correlate with an improved heat transfer rate. Rather, it signifies that the fluid's bulk temperature approximates the plate's temperature, leading to diminished heat absorption at this fluid-plate interface.

In another scenario with $\delta = -1$, where the bottom plate heats the fluid while the upper plate cools it at an equivalent rate. Here, the negative Nusselt number implies heat transfer from fluid to wall. Comparing absolute Nusselt values reveals the upper plate's Nusselt number (Nu_2) surpasses the lower plate's (Nu_2), and this difference increases with higher Hartmann numbers. This can be explained as follow: in this configuration, the fluid experiences heat input from three distinct sources. The first source is viscous dissipation, which primarily takes place in close proximity to the wall due to the high velocity gradients. The second source is Joule heating, distributed throughout the fluid's bulk with a maximum at the center core. The third source emanates from the bottom plate. The heat emanating from the bottom plates interacts with the heat from the other two sources that contributes to significant elevation in the plate temperature, hence, the reduction of the Nusselt number. Conversely, the top plate functions as the sole heat sink in this arrangement. All heat fluxes are directed towards this plate, leading to a minimization of temperature disparities between the plate and the fluid bulk, which increases the Nusselt number. At $Z = 1$ and for $Ha = 40$, $\overline{Nu_1} = 2.089$ and $|\overline{Nu_2}| = 2.263$ (denoting a + 8.3% augmentation). For the case $\delta = -2$, Nusselt number diminishes in the entry region at a given Ha number. However, in the fully developed region, plate 2's average absolute Nusselt number at $Z = 1$ increases to 2.638, while plate 1's diminishes 1.606.

The average Nusselt number has been computed at various dimensionless lengths for both plates, across different values of the heating ratio (δ), Brinkman number (Br), and the Hartmann Number (Ha). >30,000 combinations were considered, and the results are tabulated in the associated Excel file provided with this paper. These results are presented through a pivot table, allowing readers to select specific values of δ, Br, and Ha to obtain the corresponding average Nusselt number.

It has been observed that under certain circumstances, differential

heating can lead to the appearance of singularity points on the average Nusselt Number curve of either the upper or the bottom plate. For example, by using the accompanying Excel file, readers can choose parameters such as $\delta = 0.1$, $Br = 0$, and $Ha = 0.0001$ to visualize the behavior of the average Nusselt number through an interactive dynamic figure. The abrupt fluctuations in Nu_2 within the region between $Z = 10^{-2}$ and 10^{-1} can be explained as follows: As the fluid enters the microchannel with an initial temperature,θ_0, lower than the wall temperature of plate 2, θ_{w2}, it receives heat from both plates at varying rates. At some point downstream, due to the lower heating rate of plate 2, the bulk temperature of the fluid, θ_b, becomes equal then higher than the wall temperature θ_{w2}. The point where $\theta_{w2} = \theta_0$, causes $\overline{Nu_2} \rightarrow \infty$ due to the division by zero (see Eq. 15). As a result, the high values of the average Nusselt number in this particular region are meaningless.

5.2. Entropy assessment

The subsequent discussions delve into a comprehensive analysis of entropy generation within the system, including insights into how different parameters contribute to the overall thermodynamic response of the system. Fig. 5 depicts the temperature field (Fig. 5a), dimensionless entropy generation due to: heat transfer (Fig. 5b), viscous dissipation (Fig. 5c), Joule heating (Fig. 5d) and global dimensionless entropy generation (Fig. 5e), in addition to the local Bejan number (Fig. 5f), considering $Br = 1$, $Ha = 1$, $\delta = 1$, and $\eta = 1$. Notably, the axial distance is presented on a logarithmic scale. In Fig. 5a, it is evident that fluid temperature symmetrically rises downstream due to the heating process ($\delta = 1$). This figure is included to elucidate the entropy generation rate's evolution, which inherently depends on temperature. Initially, entropy generation due to heat transfer (Fig. 5b) is concentrated near the wall in the entry region, and it extend gradually towards the bulk fluid center downstream, in which significant heat transfer occurs in this region. However, further downstream, this region contracts due to the increase of the fluid temperature.

Fig. 5c depicts entropy generation due to viscous dissipation. Initially, uniform distribution prevails in the entry region due to uniform heat generation rate caused by viscous heating that depends only of velocity gradient; higher near the wall and lower at the fluid's center.

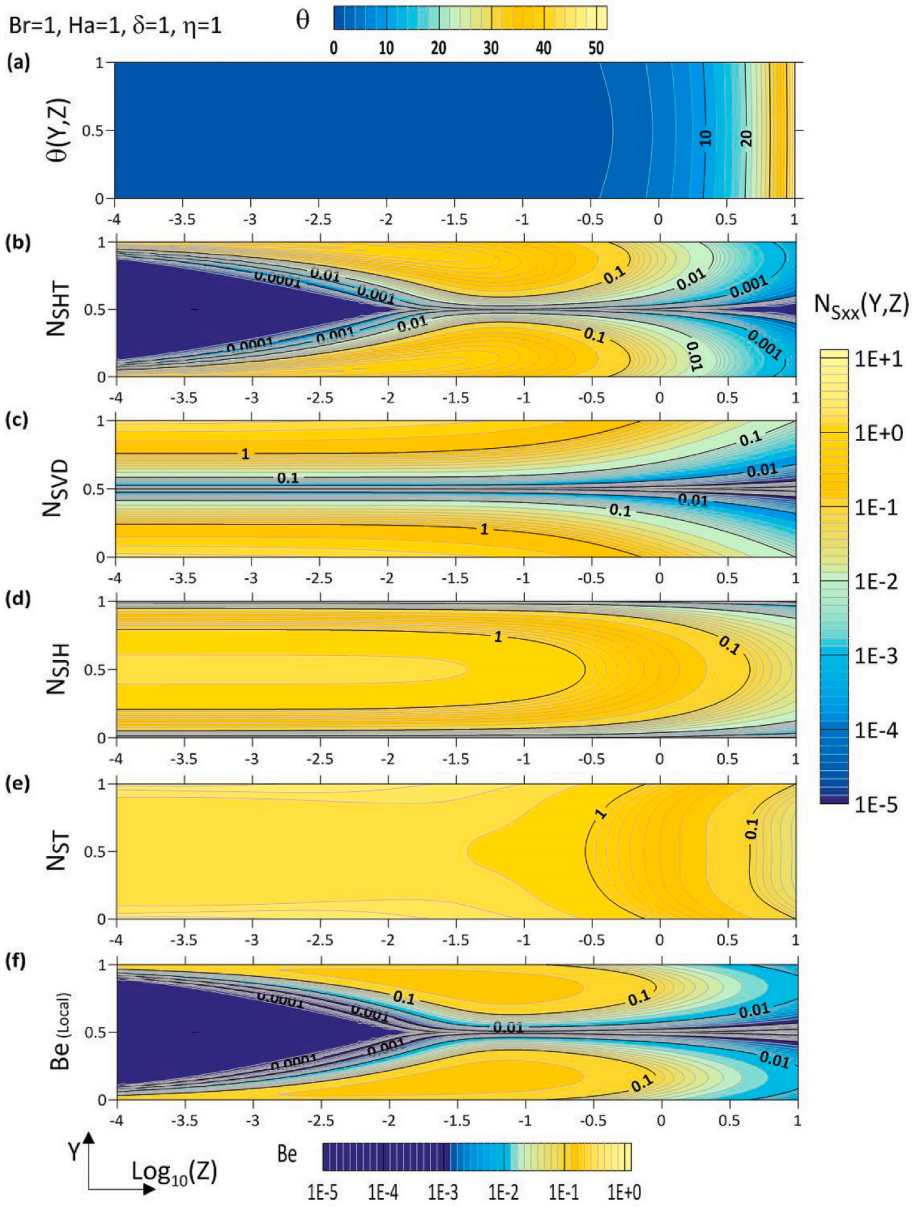

Fig. 5. Entropy Generation, Bejan Number, and Temperature Evolution Downstream.

Moving downstream, entropy rate diminishes due to fluid temperature elevation. Similar observations hold for joule heating (Fig. 5d), where entropy generation rate is uniform at the entry, and decreases downstream owing to elevated fluid temperature caused by heat transfer, and viscous and Joule heating.

The dimensionless entropy generation rate N_{ST} (Fig. 5e), being the sum of the three aforementioned entropies, follows analogous behavior - higher at entry, diminishing downstream. However, this figure does not reveal the heat transfer process contribution to entropy generation rate. Thus, the most suited parameter for clear representation is the Bejan number, as it represents the ratio of entropy generated due to heat transfer over the global entropy generation rate. Local Bejan number has been computed and depicted in Fig. 5f. The figure's shape, akin to Fig. 5b, reflects high Bejan numbers aligning with zones of high entropy generation due to heat transfer. Hence, in the forthcoming discussion, we will investigate the influence of different parameters on entropy generation, considering only the Bejan number.

Fig. 6 illustrates the impact of the dimensionless number, η, on the entropy generation rate with consideration of viscous and Joule heating. As it can be seen, for low values of η, high value of the Bejan number cover the majority of the fluid, and decreases as the value of η increases. The dimensionless parameter, η, can be regarded as a factor representing the resistance of the system to entropy generation, dependent on both the geometry (l), and the initial conditions$(T_0, \dot{q}^{''})$. A high value of η can be associated with either a low heating rate or a small channel width (l), as is often the case in micro-channels. Systems characterized by high values of η exhibit less entropy generation. Conversely, a low value of η can be associated with a high heat flux, resulting in significant entropy generation within the system.

To gain a comprehensive understanding of the influence of the parameter η, we computed the average entropy generation rates (N_{SHT}, N_{SVD}, N_{SJH}) and the average Bejan number over a wide range of η. The results are depicted in Fig. 7. It's important to note that in this case, we assumed $Br = 1$, $Ha = 1$, and $d = 1$. Additionally, we included the curve for the average N_{SHT} in the case of $Br = 0$ and $Ha = 0.0001$ with $\delta = 1$ for the purpose of comparison. As can be observed from the data, a high value of η is associated with a low entropy generation rate for all three

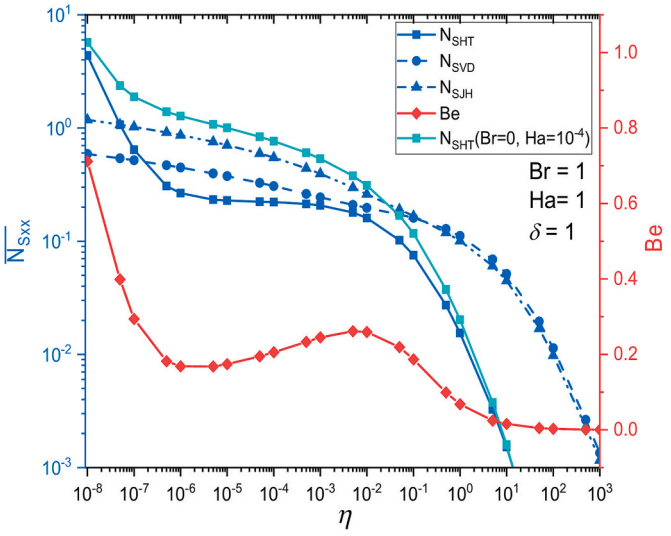

Fig. 7. Variation of average entropy generation rates and Bejan number with dimensionless parameter η.

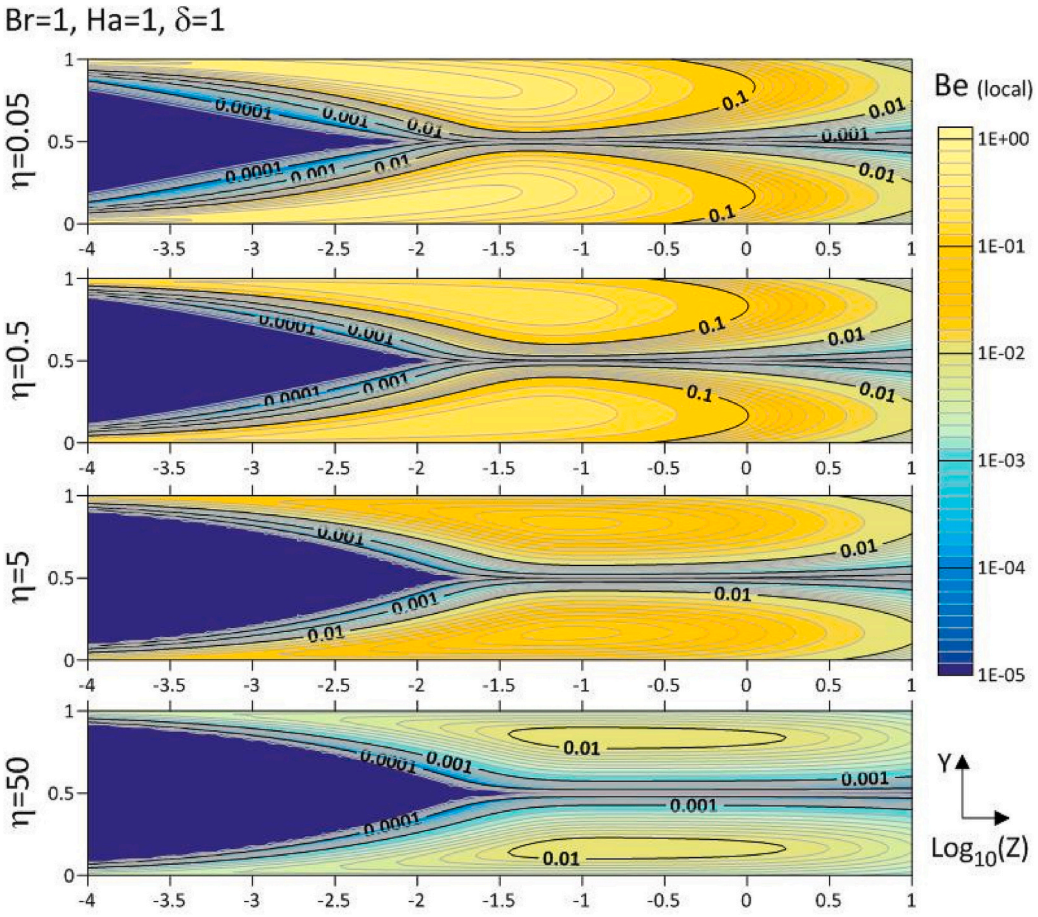

Fig. 6. Influence of dimensionless parameter η on local Bejan number.

components, as well as the average Bejan number that tends to zero. Conversely, as the value of η decreases, the entropy rates increase for all three components.

Of particular interest in the Bejan number is its initial peak at around $\eta = 10^{-2}$, where $Be = 0.26$. Following this peak, the Bejan number decreases as η decreases. Subsequently, it starts increasing again as η drops below 10^{-6}. By examining the first part of Eq. (21), we observe that the N_{SHT} component is divided by $(\theta+\eta)^2$. Since the temperature is essentially equal to zero at the entry, and as η tends to 0, this division tends towards infinity. Consequently, for η values below 10^{-6}, the increase in entropy generation and the Bejan number lose physical significance. Therefore, for systems where entropy generation cannot be avoided, maintaining η within the range of 10^{-3} to 10^{-1} is of utmost importance. In the case of micro-channels, where l is on the order of tens to hundreds micrometers, the equivalent η lies between 1 and several hundreds. This configuration results in low entropy generation within the system.

In Fig. 8, we explore the effects of differential heating and cooling on the entropy generation rate based on the local Bejan number. As evident from the figure, the ratio δ has a significant impact on entropy generation. This effect becomes noticeable when one plate heats while the other cools ($\delta = -2$ and -1), resulting in notably high entropy generation rates in terms of the local Bejan number. This phenomenon arises due to the considerable temperature gradient existing between the two plates. For the scenario where the top plate is isolated ($\delta = 0$), we can observe a concentration of high local Bejan numbers near the bottom plate, attributed to heat transfer between the wall and the fluid, whereas low local *Be* are localized near the isolated wall. In cases where both plates heat up, albeit at different rates ($\delta = 0.5$), an unbalanced distribution of the local Bejan number emerges, characterized by a high Bejan number near the bottom plate and a low Bejan number near the top plate.

The practical implications of these findings are contingent upon the specific system in question. Consider, for instance, the situation where we aim to dissipate the heat generated by plate 1. If we possess a heat sink (represented as plate 2) capable of dissipating the heat produced by plate 1, the introduction of a film fluid between the surface and the sink becomes redundant. This is due to the high entropies generated by the fluid, which in turn renders the system inefficient. In this context, a more practical approach involves placing the heat sink directly in contact with the heat source.

In another scenario, we might encounter a situation where the isolation of plate 2 is inadequate. Heat evacuated by plate 2 could then be perceived as a heat loss from the system to the environment. These heat losses contribute to entropy generation, thereby leading to elevated values of the Bejan number. Similarly, when heat flows into the system due to poor isolation and a hot environment, this circumstance also contributes to the rate of entropy generation.

Fig. 9 provides a summary of the average Bejan number for the system across various values of *Br*, *Ha*, δ, and η. It is important to note that in certain cases, such as when $Br = 0.01$ and $\eta = 0.01$, the presence of zigzag contours can be observed. These contours arise from the plotting method employed by third-party software to generate contours and lack significant physical implications. One notable observation is that the local Bejan number diminishes as the Hartmann number and/or

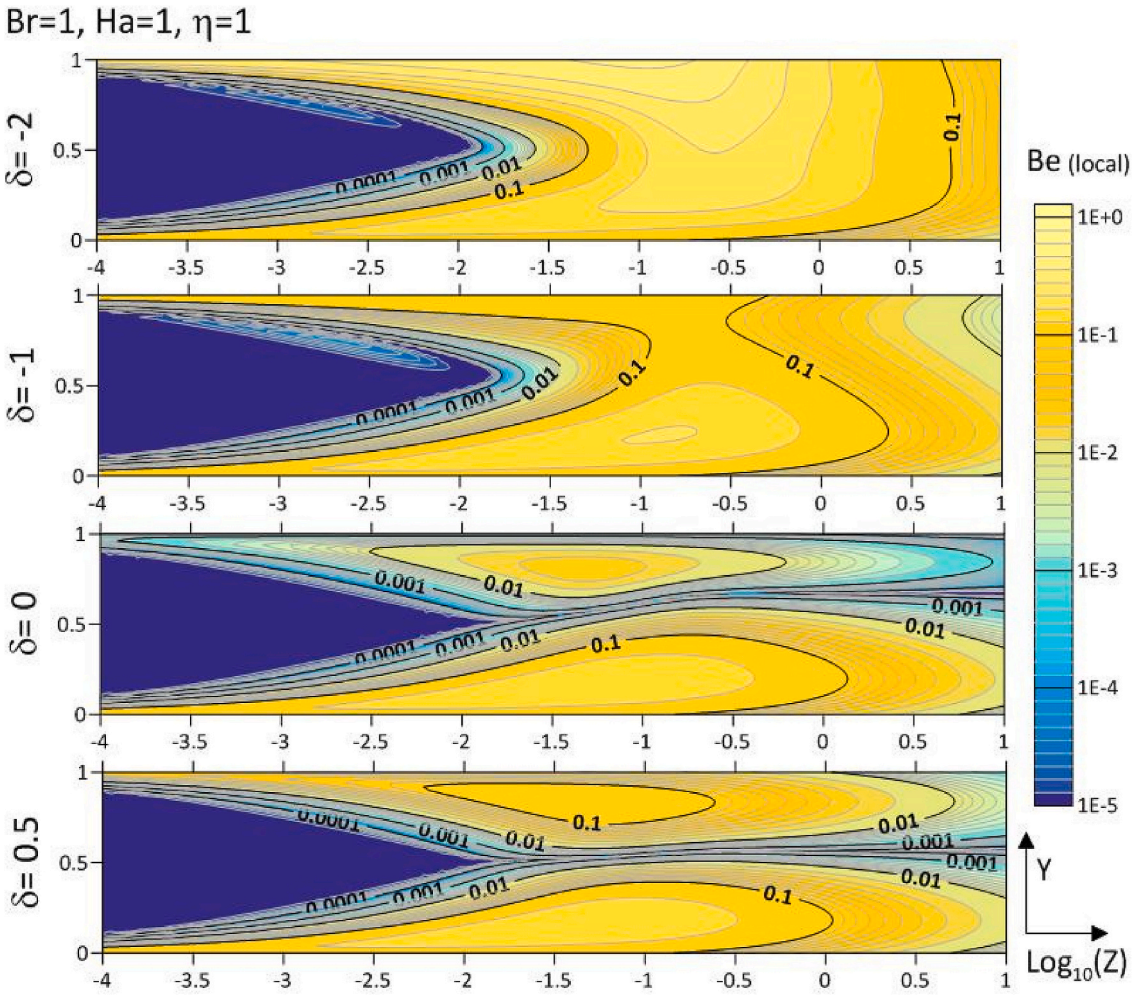

Fig. 8. Effect of heat flux ratio, δ, on entropy the local Bejan number.

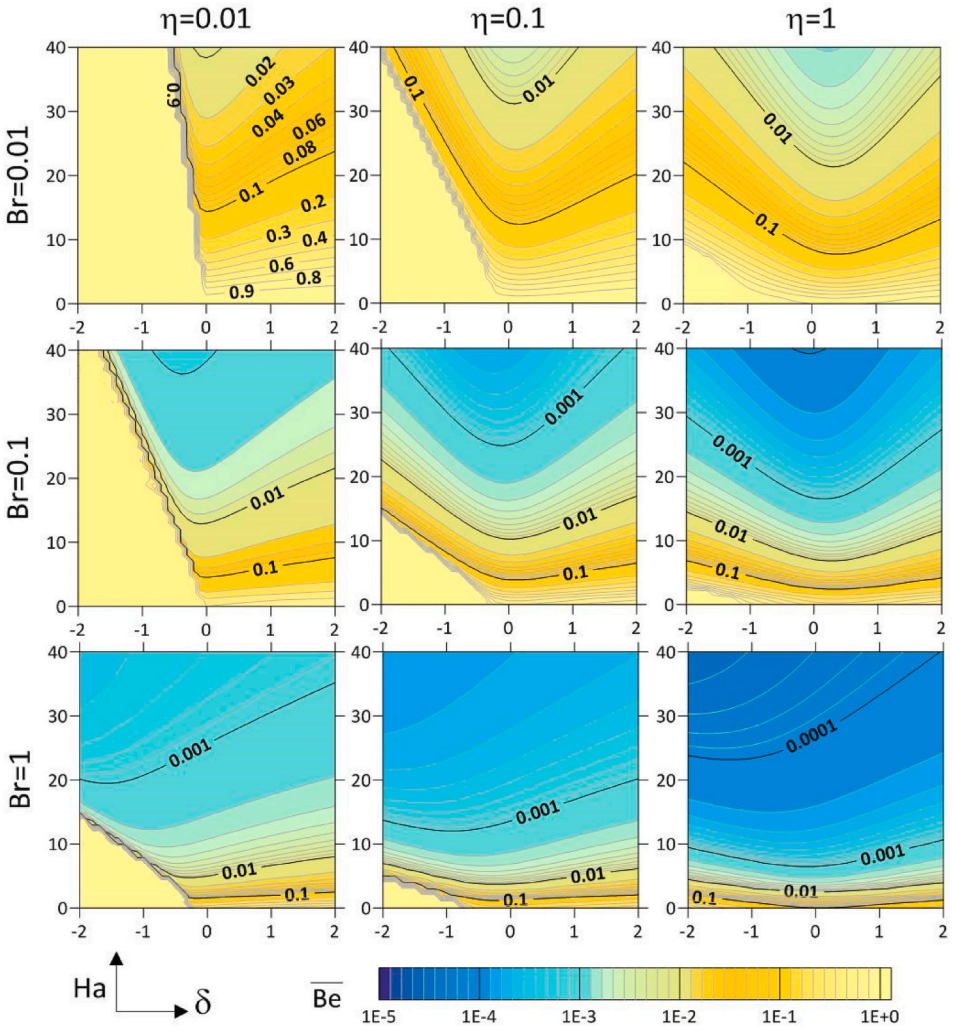

Fig. 9. Average Bejan number variation with *Br*, *Ha*, δ, and η in a micro-channel with length $Z = 10$.

the Brinkman number increases. This decrease can be attributed to the augmentation in heat generation due to either/both viscous dissipation and Joule heating. Furthermore, it becomes evident that for a given Hartmann number, the system's minimum average Bejan number occurs at approximately $\delta = 0$. The value of *Be* increases as the magnitude of δ deviates from zero. However, the rate of increase varies, whether positive or negative. In addition, it is especially remarkable the substantial rate of increase in the Bejan number when plate 2 is subjected to cooling. This phenomenon is driven by the presence of a high temperature gradient, as discussed earlier, and in various cases, this increase leads to the Bejan number attaining a value of $Be = 1$.

6. Conclusion

This study investigates the heat transfer and entropy generation dynamics within a magneto-hydrodynamic fluid flow (MHD), in a microchannel, under the influence of differential heating, viscous dissipation and Joule heating. The numerical solution strategy employs a finite difference method along with a fully implicit scheme to discretize the governing equations. This approach accurately captures the temperature field and subsequent entropy generation. The developed in-house code's reliability is rigorously established through mesh sensitivity analyses and extensive comparisons with analytical solutions and literature data. The main findings are:

- Heat transfer analysis reveals subtle fluctuations in the heat transfer rate, influenced by factors such as viscous dissipation, Joule heating, Hartmann number, Brinkman number, and heating ratio.
- The comparison between the average Nusselt number calculated using the classical formula and the Bennett Formula [48] demonstrates a significant deviation, particularly noticeable at the entry length, with potential errors of up to 14%. This has critical implications for engineering applications, leading to the computation of average Nusselt numbers for over 30,000 combinations of Br, Ha, and δ at various axial positions, with detailed results provided in the accompanying spreadsheet.
- When one plate is subjected to heating while the other plate is cooled, and the Hartmann number is at a low level, the average Nusselt number for both plates approaches 2. Nevertheless, at elevated *Ha* values, taking into account viscous dissipation and Joule heating, an 8% disparity emerges between the Nusselt numbers of the two plates, with the cooling plate exhibiting the higher *Nu* value.
- Entropy assessment highlights the sensitivity of dimensionless entropy generation rates to controlling parameters like *Br*, *Ha*, and δ. Within the dimensionless entropy formulation, the parameter η emerges as a significant factor affecting entropy generation rates.
- Higher η values correspond to lower entropy generation, underscoring its role in entropy minimization. Increasing η form 0.1 to 0.5 reduces the entropy generation rate by 32%.
- For Micro Channels, it's noteworthy that they typically exhibit higher δ values by default, and substantial high η values imply reduced

entropy generation, underscoring their high efficiency in heat transfer.

In essence, the findings reveal the delicate balance between heat transfer and entropy generation in microscale systems subjected to differential heating.

CRediT authorship contribution statement

Haroun Ragueb: Conceptualization, Methodology, Software, Validation, Investigation, Writing – original draft, Writing – review & editing. **Antar Tahiri:** Conceptualization, Methodology, Software, Investigation, Writing – original draft. **Dounya Behnous:** Software, Writing – review & editing, Investigation. **Belkacem Manser:** Software, Writing – review & editing. **Kamel Rachedi:** Software, Validation, Investigation. **Kacem Mansouri:** Conceptualization, Supervision, Writing – review & editing.

Declaration of Competing Interest

The authors declare that they have no known competing financial interests or personal relationships that could have appeared to influence the work reported in this paper.

Data availability

Data will be made available on request.

References

[1] B. Dash, J. Nanda, S.K. Rout, The role of microchannel geometry selection on heat transfer enhancement in heat sinks: a review, Heat Transf. 51 (2022) 1406–1424, https://doi.org/10.1002/htj.22357.

[2] K. Pawel, W. Rafal, Microsensors for microreaction and lab-on-a-chip applications, in: M. Igor (Ed.), Microsensors, IntechOpen, Rijeka, 2011 pp. Ch. 5.

[3] S. Litster, Micropumps, in: B. Bhushan (Ed.), Encyclopedia of Nanotechnology, Springer, Netherlands, Dordrecht, 2012, pp. 1430–1436.

[4] O.K. Siddiqui, S.M. Zubair, Efficient energy utilization through proper design of microchannel heat exchanger manifolds: a comprehensive review, Renew. Sust. Energ. Rev. 74 (2017) 969–1002, https://doi.org/10.1016/j.rser.2017.01.074.

[5] H. Ge-JiLe, S. Qayyum, F. Shah, M.I. Khan, S.U. Khan, Slip flow of Jeffrey nanofluid with activation energy and entropy generation applications, Adv. Mech. Eng. 13 (2021), https://doi.org/10.1177/16878140211006578, 16878140211006578.

[6] M.I. Khan, S. Qayyum, S. Kadry, W. Khan, S. Abbas, Theoretical investigations of entropy optimization in electro-magneto nonlinear mixed convective second order slip flow, J. Mag. 25 (2020) 8–14, https://doi.org/10.4283/JMAG.2020.25.1.008.

[7] S.S. Antman, J.E. Marsden, L. Sirovich, Basic concepts and technologies, in: Microflows and Nanoflows: Fundamentals and Simulation, Springer, New York, New York, NY, 2005, pp. 1–48.

[8] S.S. Antman, J.E. Marsden, L. Sirovich, Numerical methods for continuum simulation, in: Microflows and Nanoflows: Fundamentals and Simulation, Springer, New York, New York, NY, 2005, pp. 509–558.

[9] H. Ragueb, K. Mansouri, Exact solution of the Graetz–Brinkman problem extended to non-Newtonian nanofluids flow in elliptical microchannels, J. Eng. Math. 140 (2023) 10, https://doi.org/10.1007/s10665-023-10267-6.

[10] O.M. Al-Habahbeh, M. Al-Saqqa, M. Safi, T. Abo Khater, Review of magnetohydrodynamic pump applications, Alex. Eng. J. 55 (2016) 1347–1358, https://doi.org/10.1016/j.aej.2016.03.001.

[11] S. Ahmad, T. Hayat, A. Alsaedi, H. Ullah, F. Shah, Computational modeling and analysis for the effect of magnetic field on rotating stretched disk flow with heat transfer, Propulsion Power Res. 10 (2021) 48–57, https://doi.org/10.1016/j.jppr.2020.11.005.

[12] T. Hayat, F. Shah, M.I. Khan, A. Alsaedi, T. Yasmeen, Modeling MHD stagnation point flow of thixotropic fluid with non-uniform heat absorption/generation, Microgr. Sci. Technol. 29 (2017) 459–465, https://doi.org/10.1007/s12217-017-9564-7.

[13] T. Hayat, F. Shah, A. Alseadi, Cattaneo-Christov double diffusions and entropy generation in MHD second grade nanofluid flow by a Riga wall, Int. Commun. Heat Mass Transf. 119 (2020), 104824, https://doi.org/10.1016/j.icheatmasstransfer.2020.104824.

[14] A. Hamid, R. Naveen Kumar, R.J. Punith Gowda, R.S. Varun Kumar, S.U. Khan, M. Ijaz Khan, B.C. Prasannakumara, T. Muhammad, Impact of Hall current and homogenous–heterogenous reactions on MHD flow of GO-MoS2/water (H2O)-ethylene glycol (C2H6O2) hybrid nanofluid past a vertical stretching surface, Waves Random Complex Media (2021) 1–18, https://doi.org/10.1080/17455030.2021.1985746.

[15] M. Qin, H.H. Bau, When MHD-based microfluidics is equivalent to pressure-driven flow, Microfluid. Nanofluid. 10 (2011) 287–300, https://doi.org/10.1007/s10404-010-0668-2.

[16] B. Jian-Bin, D.J. Harrison, Design and fabrication of microchannels for magnetohydrodynamic flow, in: Proceedings International Conference on MEMS, NANO and Smart Systems, 2003, pp. 396–399.

[17] H. Nakagawa, M. Ohuchi, Artificial blood-flow controlling effects of inhomogeneity of twisted magnetic fields, J. Magn. Magn. Mater. 431 (2017) 273–276, https://doi.org/10.1016/j.jmmm.2016.10.003.

[18] S. Morteza Mousavi, B. Ehteshami, A. Ali Rabienataj Darzi, Two-and-three-dimensional analysis of Joule and viscous heating effects on MHD nanofluid forced convection in microchannels, Thermal Sci. Eng. Prog. 25 (2021), 100983, https://doi.org/10.1016/j.tsep.2021.100983.

[19] M. Li, L. Zhang, H. Hassanzadeh Afrouzi, A. Abouei Mehrizi, A comprehensive investigation of nanofluid conjugate heat transfer in a microchannel under MHD effect, Alex. Eng. J. 80 (2023) 506–519, https://doi.org/10.1016/j.aej.2023.08.075.

[20] A.T. Akinshilo, Mixed convective heat transfer analysis of MHD fluid flowing through an electrically conducting and non-conducting walls of a vertical micro-channel considering radiation effect, Appl. Therm. Eng. 156 (2019) 506–513, https://doi.org/10.1016/j.applthermaleng.2019.04.100.

[21] A. Hajatzadeh Pordanjani, A. Raisi, A. Daneh-Dezfuli, Slip and non-slip flows of MHD nanofluid through microchannel to cool discrete heat sources in presence and absence of viscous dissipation, J. Magn. Magn. Mater. 580 (2023), 170972, https://doi.org/10.1016/j.jmmm.2023.170972.

[22] M. Kalteh, S.S. Abedinzadeh, Numerical investigation of MHD nanofluid forced convection in a microchannel using lattice Boltzmann method, Iranian journal of science and technology, transactions of, Mech. Eng. 42 (2018) 23–34, https://doi.org/10.1007/s40997-017-0073-5.

[23] M. Ebrahim Qomi, G.A. Sheikhzadeh, A. Fattahi, Heat transfer enhancement in a microchannel using a pulsating MHD hybrid nanofluid flow, Energy Sour. Part A (2020) 1–16, https://doi.org/10.1080/15567036.2020.1834031.

[24] A.Y. Sayed, S.I. Ahmed, K.S. Mekheimer, M.S. Abdel-wahed, Electromagnetohydrodynamic effects with single-walled carbon nanotubes particles in a corrugated microchannel, Chaos, Solitons Fractals 168 (2023), 113126, https://doi.org/10.1016/j.chaos.2023.113126.

[25] B.J. Gireesha, S. Sindhu, G. Sowmya, A. Felicita, Magnetohydrodynamic flow of Williamson fluid in a microchannel for both horizontal and inclined loci with wall shear properties, Heat Transf. 50 (2021) 1428–1442, https://doi.org/10.1002/htj.21937.

[26] C. Yang, Y. Jian, Z. Xie, F. Li, Heat transfer characteristics of magnetohydrodynamic electroosmotic flow in a rectangular microchannel, Eur. J. Mech. - B/Fluids 74 (2019) 180–190, https://doi.org/10.1016/j.euromechflu.2018.11.015.

[27] A. Bejan, Entropy Generation Minimization: The Method of Thermodynamic Optimization of Finite-Size Systems and Finite-Time Processes, 1st ed., CRC Press, 1995.

[28] Y. Haseli, Performance of irreversible heat engines at minimum entropy generation, Appl. Math. Model. 37 (2013) 9810–9817, https://doi.org/10.1016/j.apm.2013.05.010.

[29] J. Gonzalez-Ayala, A. Calvo Hernández, J.M.M. Roco, From maximum power to a trade-off optimization of low-dissipation heat engines: influence of control parameters and the role of entropy generation, Phys. Rev. E 95 (2017), 022131, https://doi.org/10.1103/PhysRevE.95.022131.

[30] M.I. Khan, S. Qayyum, T. Hayat, M. Waqas, M.I. Khan, A. Alsaedi, Entropy generation minimization and binary chemical reaction with Arrhenius activation energy in MHD radiative flow of nanomaterial, J. Mol. Liq. 259 (2018) 274–283, https://doi.org/10.1016/j.molliq.2018.03.049.

[31] M.I. Khan, F. Alzahrani, A. Hobiny, Z. Ali, Estimation of entropy generation in Carreau-Yasuda fluid flow using chemical reaction with activation energy, J. Mater. Res. Technol. 9 (2020) 9951–9964, https://doi.org/10.1016/j.jmrt.2020.05.085.

[32] Y.-M. Chu, F. Shah, M.I. Khan, S. Kadry, Z. Abdelmalek, W.A. Khan, Cattaneo-Christov double diffusions (CCDD) in entropy optimized magnetized second grade nanofluid with variable thermal conductivity and mass diffusivity, J. Mater. Res. Technol. 9 (2020) 13977–13987, https://doi.org/10.1016/j.jmrt.2020.09.101.

[33] T. Hayat, F. Shah, A. Alsaedi, B. Ahmad, Entropy optimized dissipative flow of effective Prandtl number with melting heat transport and Joule heating, Int. Commun. Heat Mass Transf. 111 (2020), 104454, https://doi.org/10.1016/j.icheatmasstransfer.2019.104454.

[34] F. Shah, T. Hayat, A. Alsaedi, Entropy optimization in a fourth grade nanofluid flow over a stretchable Riga wall with thermal radiation and viscous dissipation, Int. Commun. Heat Mass Transf. 127 (2021), 105398, https://doi.org/10.1016/j.icheatmasstransfer.2021.105398.

[35] Y.-M. Chu, M. Nazeer, M.I. Khan, W. Ali, Z. Zafar, S. Kadry, Z. Abdelmalek, Entropy analysis in the Rabinowitsch fluid model through inclined Wavy Channel: constant and variable properties, Int. Commun. Heat Mass Transf. 119 (2020), 104980, https://doi.org/10.1016/j.icheatmasstransfer.2020.104980.

[36] V. Puttaswmay, G. Bijjanal Jayanna, S. Doranalu Onkarappa, Heat transfer and irreversibility rate in MHD flow of a hybrid nanofluid with Newton boundary condition, slip flow, and nonlinear thermal radiation, Heat Transf. 50 (2021) 3342–3365, https://doi.org/10.1002/htj.22031.

[37] B. Gireesha, C. Srinivasa, N. Shashikumar, M. Macha, J. Singh, B. Mahanthesh, Entropy generation and heat transport analysis of Casson fluid flow with viscous and Joule heating in an inclined porous microchannel, Proc. Inst. Mech. Eng. Part E. 233 (2019) 1173–1184, https://doi.org/10.1177/0954408919849987.

[38] S.R. Hosseini, M. Ghasemian, M. Sheikholeslami, A. Shafee, Z. Li, Entropy analysis of nanofluid convection in a heated porous microchannel under MHD field considering solid heat generation, Powder Technol. 344 (2019) 914–925, https://doi.org/10.1016/j.powtec.2018.12.078.
[39] M. Waleed Ahmad Khan, M. Ijaz Khan, T. Hayat, A. Alsaedi, Numerical solution of MHD flow of power law fluid subject to convective boundary conditions and entropy generation, Comput. Methods Prog. Biomed. 188 (2020), 105262, https://doi.org/10.1016/j.cmpb.2019.105262.
[40] M. Madhu, B. Mahanthesh, N.S. Shashikumar, S.A. Shehzad, S.U. Khan, B. J. Gireesha, Performance of second law in Carreau fluid flow by an inclined microchannel with radiative heated convective condition, Int. Commun. Heat Mass Transf. 117 (2020), 104761, https://doi.org/10.1016/j.icheatmasstransfer.2020.104761.
[41] M. Madhu, N.S. Shashikumar, B. Mahanthesh, B.J. Gireesha, N. Kishan, Heat transfer and entropy generation analysis of non-Newtonian flu flow through vertical microchannel with convective boundary condition, Appl. Math. Mech. 40 (2019) 1285–1300, https://doi.org/10.1007/s10483-019-2516-9.
[42] S. Noreen, S. Waheed, D.C. Lu, A. Hussanan, Entropy generation in electromagnetohydrodynamic water based three Nano fluids via porous asymmetric microchannel, Eur. J. Mech. - B/Fluids 85 (2021) 458–466, https://doi.org/10.1016/j.euromechflu.2020.11.002.
[43] D.P.C. Rao, M.J. Babu, S.A. Shehzad, S. Qaisar, Entropy generation optimization in a radiative hybrid nanofluid (engine oil + NiZnFe2O4 + MnZnFe2O4) flow through a convectively heated microchannel with cross-diffusion effects, J. Therm. Anal. Calorim. (2023), https://doi.org/10.1007/s10973-023-12412-w.
[44] M.A. Jamil, S.Z. Shuja, S.M. Zubair, Selection of optimum heat flux distribution in pipe flow under laminar forced convection, Arab. J. Sci. Eng. 46 (2021) 2177–2190, https://doi.org/10.1007/s13369-020-05053-w.
[45] G. Ibáñez, S. Cuevas, Entropy generation minimization of a MHD (magnetohydrodynamic) flow in a microchannel, Energy 35 (2010) 4149–4155, https://doi.org/10.1016/j.energy.2010.06.035.
[46] L.H. Back, Laminar heat transfer in electrically conducting fluids flowing in parallel plate channels, Int. J. Heat Mass Transf. 11 (1968) 1621–1636, https://doi.org/10.1016/0017-9310(68)90043-4.
[47] S.M. Aminossadati, A. Raisi, B. Ghasemi, Effects of magnetic field on nanofluid forced convection in a partially heated microchannel, Int. J. Non-Linear Mech. 46 (2011) 1373–1382, https://doi.org/10.1016/j.ijnonlinmec.2011.07.013.
[48] T.D. Bennett, A historical misperception on calculating the average convection coefficient in tubes with constant wall heat flux, J. Heat Transf. 141 (2019), https://doi.org/10.1115/1.4043303.
[49] T.D. Bennett, Correlations for the Graetz problem in convection – part 1: for round pipes and parallel plates, Int. J. Heat Mass Transf. 136 (2019) 832–841, https://doi.org/10.1016/j.ijheatmasstransfer.2019.03.006.
[50] A. Bejan, Second-law analysis in heat transfer and thermal design, in: J.P. Hartnett, T.F. Irvine (Eds.), Advances in Heat Transfer, Elsevier, 1982, pp. 1–58.
[51] G. Qin, Computational Fluid Dynamics for Mechanical Engineering, CRC Press, London, England, 2021.
[52] F. Suárez-Carreño, L. Rosales-Romero, Convergency and stability of explicit and implicit schemes in the simulation of the heat equation, Appl. Sci. 11 (2021) 4468, https://doi.org/10.3390/app11104468.
[53] H. Ragueb, K. Mansouri, Numerical investigation of laminar forced convection for a non-Newtonian nanofluids flowing inside an elliptical duct under convective boundary condition, Int. J. Num. Methods Heat Fluid Flow 29 (2019) 334–364, https://doi.org/10.1108/HFF-02-2018-0055.
[54] R.M. Cotta, M.N. Özişik, Laminar forced convection to non-Newtonian fluids in ducts with prescribed wall heat flux, Int. Commun. Heat Mass Transf. 13 (1986) 325–334, https://doi.org/10.1016/0735-1933(86)90020-5.
[55] J. Lahjomri, K. Zniber, A. Oubarra, A. Alemany, Heat transfer by laminar Hartmann's flow in thermal entrance region with uniform wall heat flux: the Graetz problem extended, Energy Convers. Manag. 44 (2003) 11–34, https://doi.org/10.1016/S0196-8904(02)00048-1.
[56] J. Sheela-Francisca, C.P. Tso, Viscous dissipation effects on parallel plates with constant heat flux boundary conditions, Int. Commun. Heat Mass Transf. 36 (2009) 249–254, https://doi.org/10.1016/j.icheatmasstransfer.2008.11.003.